

# Implementation of a High-Accuracy Finite-Difference Scheme for Linear Wave Phenomena

H.M. Jurgens\*

D.W. Zingg†

## Abstract

A high-accuracy finite-difference scheme is used to solve the two-dimensional time-domain Maxwell equations governing the propagation and scattering of electromagnetic waves. The scheme uses a seven-point spatial operator with an explicit six-stage time-marching method of Runge-Kutta type. Boundary formulations are given for perfect conductors and interfaces between dielectric media with differing permittivities. Numerical experiments are performed for pulsed plane waves incident on a dielectric square and a perfectly-conducting cylinder using Cartesian and curvilinear grids, respectively. The results demonstrate the general usefulness of the high-accuracy scheme and its superior efficiency relative to a second-order scheme.

**Key words:** finite-difference schemes, wave propagation, Maxwell's equations.

**AMS subject classifications:** 65M05, 76-08, 78-08.

## 1 Introduction

One of the more promising areas of application of high-order finite-difference methods is in the numerical simulation of wave phenomena, which has recently become an area of considerable interest. Future prospects in computational electromagnetics and aeroacoustics are discussed in Refs. [9] and [7], respectively. Numerous researchers have demonstrated the inadequacy of low-order finite-difference methods for accurate simulation of long-range wave propagation with reasonable grid densities. Consequently, several high-accuracy finite-difference schemes have recently

been developed specifically for simulating wave phenomena [2, 3, 6, 8, 10, 13, 14]. In general, these new schemes are analysed in a one-dimensional context or in two dimensions on square grids. However, in most practical problems of interest involving waves, scattering phenomena are important. The geometry of the scattering object can be complex. Consequently, the numerical formulation of boundary and interface conditions for complex geometries is an important aspect of high-accuracy schemes for simulating wave phenomena.

There are three basic approaches for applying a finite-difference or similar method to complex geometries: Cartesian (or rectilinear) grids, curvilinear grids, and unstructured grids. Cartesian grids have several advantages. Finite-difference schemes are typically most accurate on a regular grid. Furthermore, generation of Cartesian grids is relatively straightforward. In contrast, generation of curvilinear grids can require considerable effort. For complex geometries, multiple curvilinear grids are usually required, either patched together or overlapping. The major advantage of curvilinear grids is in the treatment of boundaries and interfaces, which normally lie along grid lines. Cartesian grids require complicated boundary treatments, especially if high-order accuracy is to be maintained. Unstructured grids, which are normally associated with finite-element methods, are often less expensive to generate than curvilinear grids. However, higher-order accuracy can be difficult to obtain. The finite-difference methods presented in Refs. [2, 3, 6, 8, 10, 13, 14] cannot be used with unstructured grids.

Based on Fourier error analysis, the finite-difference scheme presented in Refs. [13] and [14] is among the most promising for simulating linear wave phenomena [15]. It is intended for simulations in which high accuracy is required for waves being propagated over relatively large distances. The scheme produces dissipative and dispersive errors which are of roughly equal magnitude. Accurate results can be obtained for waves propagating over five hundred wavelengths with less than seventeen grid points per wavelength. This result, obtained using Fourier error analysis, applies to wave propagation on uniform Cartesian

\*Ph.D. candidate, Institute for Aerospace Studies, University of Toronto, 4925 Dufferin St., Downsview, Ont., Canada M3H 5T6

†Associate Professor, same address

grids without reflection or other scattering phenomena. There has been little research on the impact of nonuniform and curvilinear grids on the accuracy of such methods.

In this paper, the high-accuracy finite-difference scheme presented in Refs. [13] and [14] is applied to two problems involving the propagation and scattering of electromagnetic waves. The first involves a pulsed plane wave incident on a dielectric square, the second involves a pulsed plane wave incident on a perfectly conducting cylinder. The dielectric square permits the straightforward application of a Cartesian grid while a curvilinear grid is used for the cylinder. The objectives of the present work are 1) to demonstrate the usefulness of the present boundary formulations for perfect conductors and interfaces between dielectric media with different permittivities, and 2) to compare the efficiency of the high-accuracy finite-difference scheme with that of lower-order schemes for problems involving scattering and curvilinear grids. Although the emphasis here is on electromagnetic waves, the finite-difference scheme, the boundary formulations, and the conclusions are equally applicable to acoustic and elastic waves. The paper is organized in the following manner. First, the Maxwell equations are given. Next, the finite-difference scheme is presented, including the spatial operator and the time-marching method. The interface formulations are then described. Finally, numerical results for the two test problems are presented and some conclusions are drawn.

## 2 Governing equations

The Maxwell equations governing electromagnetic waves are:

$$(1) \quad \nabla \cdot \mathbf{D} = \rho$$

$$(2) \quad \nabla \cdot \mathbf{B} = 0$$

$$(3) \quad \nabla \times \mathbf{E} = -\frac{\partial \mathbf{B}}{\partial t}$$

$$(4) \quad \nabla \times \mathbf{H} = \mathbf{J} + \frac{\partial \mathbf{D}}{\partial t}$$

where  $\mathbf{E}$  and  $\mathbf{H}$  are the electric and magnetic field intensities,  $\mathbf{D}$  and  $\mathbf{B}$  are the electric and magnetic flux densities,  $\mathbf{J}$  is the current density and  $\rho$  is the charge density. The constitutive relations are:

$$(5) \quad \mathbf{D} = \epsilon \mathbf{E}$$

$$(6) \quad \mathbf{B} = \mu \mathbf{H}$$

where  $\epsilon$  is the electric permittivity and  $\mu$  is the magnetic permeability. We restrict our attention to linear isotropic

homogeneous non-conducting media with no charge density ( $\rho = 0$ ). Under these conditions,  $\epsilon$  and  $\mu$  are positive real scalar constants and  $\mathbf{J} = 0$ . We consider a nondimensional form of the equations such that  $\epsilon = \mu = 1$  in free space. Furthermore, we assume that the initial conditions and any incoming waves satisfy the divergence relations. Hence these relations need not be enforced numerically.

In two dimensions, the Maxwell equations can be decoupled into two sets of equations, the transverse magnetic (TM) set involving the  $z$  component of the electric field and the  $x$  and  $y$  components of the magnetic field, and the transverse electric (TE) set involving the  $x$  and  $y$  components of the electric field and the  $z$  component of the magnetic field. Without any loss of physics, we will consider only the TM formulation, which can be written as

$$(7) \quad \frac{\partial \mathbf{Q}}{\partial t} + \tilde{\mathbf{A}} \frac{\partial \mathbf{Q}}{\partial x} + \tilde{\mathbf{B}} \frac{\partial \mathbf{Q}}{\partial y} = 0$$

where

$$\mathbf{Q} = \begin{bmatrix} D_z \\ B_x \\ B_y \end{bmatrix},$$

$$\tilde{\mathbf{A}} = \begin{bmatrix} 0 & 0 & -1/\mu \\ 0 & 0 & 0 \\ -1/\epsilon & 0 & 0 \end{bmatrix},$$

$$\tilde{\mathbf{B}} = \begin{bmatrix} 0 & 1/\mu & 0 \\ 1/\epsilon & 0 & 0 \\ 0 & 0 & 0 \end{bmatrix},$$

and  $D_z$ ,  $B_x$ , and  $B_y$  are Cartesian components of  $\mathbf{D}$  and  $\mathbf{B}$ , respectively. The above equation assumes constant material properties. If the material properties are spatially varying, then source terms are introduced.

In order to apply a finite-difference method, the domain must be discretized using a grid. With a rectilinear grid, the above equations can be discretized directly. With a curvilinear grid, the equations are transformed into a rectilinear computational space. The Cartesian coordinates are mapped to curvilinear coordinates  $\xi(x, y)$ ,  $\eta(x, y)$  such that the resulting grid is uniform and square with  $\Delta\xi = \Delta\eta = 1$ . In general, the mapping is defined by assigning integer curvilinear coordinate values to each grid node, although an analytical mapping can be used for some geometries. The transformed equation is

$$(8) \quad \frac{\partial \mathbf{Q}}{\partial t} + \tilde{\mathbf{A}} \frac{\partial \xi}{\partial x} \frac{\partial \mathbf{Q}}{\partial \xi} + \tilde{\mathbf{A}} \frac{\partial \eta}{\partial x} \frac{\partial \mathbf{Q}}{\partial \eta} + \tilde{\mathbf{B}} \frac{\partial \xi}{\partial y} \frac{\partial \mathbf{Q}}{\partial \xi} + \tilde{\mathbf{B}} \frac{\partial \eta}{\partial y} \frac{\partial \mathbf{Q}}{\partial \eta} = 0$$

The metrics of the transformation can be found numerically if no analytical mapping is available. For details see, for example, Ref. [1]. Equation 8 can be rewritten in the following form:

$$(9) \quad \frac{\partial \mathbf{Q}}{\partial t} + \hat{\mathbf{A}} \frac{\partial \mathbf{Q}}{\partial \xi} + \hat{\mathbf{B}} \frac{\partial \mathbf{Q}}{\partial \eta} = 0$$

where

$$(10) \quad \hat{\mathbf{A}} = \begin{bmatrix} 0 & \frac{1}{\mu} \frac{\partial \xi}{\partial y} & -\frac{1}{\mu} \frac{\partial \xi}{\partial x} \\ \frac{1}{\epsilon} \frac{\partial \xi}{\partial y} & 0 & 0 \\ -\frac{1}{\epsilon} \frac{\partial \xi}{\partial x} & 0 & 0 \end{bmatrix}$$

and

$$(11) \quad \hat{\mathbf{B}} = \begin{bmatrix} 0 & \frac{1}{\mu} \frac{\partial \eta}{\partial y} & -\frac{1}{\mu} \frac{\partial \eta}{\partial x} \\ \frac{1}{\epsilon} \frac{\partial \eta}{\partial y} & 0 & 0 \\ -\frac{1}{\epsilon} \frac{\partial \eta}{\partial x} & 0 & 0 \end{bmatrix}.$$

### 3 Numerical method

Our objective is to solve for the total electric and magnetic field intensities within dielectric media for arbitrary waves entering the computational domain. The high-accuracy finite-difference scheme of Refs. [13] and [14] consists of a seven-point spatial operator together with an explicit six-stage time-marching method of Runge-Kutta type. The spatial operator is divided into an antisymmetric component, i.e., a centered difference operator, and a symmetric component, which provides a small amount of dissipation. The symmetric component is added to provide stability and to damp spurious high wavenumber components of the solution. A detailed analysis of the method, including stability and error analysis is given in Refs. [13] and [14].

On a uniform grid with  $x_j = j\Delta x$ , the antisymmetric component of the spatial operator is

$$(12) \quad (\delta_x^a u)_j = \frac{1}{\Delta x} [a_3 (u_{j+3} - u_{j-3}) + a_2 (u_{j+2} - u_{j-2}) + a_1 (u_{j+1} - u_{j-1})]$$

where  $a_1 = 3/4$ ,  $a_2 = -3/20$ ,  $a_3 = 1/60$ , and  $u_j = u(x_j)$ . The symmetric component is

$$(13) \quad (\delta_x^s u)_j = \frac{1}{\Delta x} [d_3 (u_{j+3} + u_{j-3}) + d_2 (u_{j+2} + u_{j-2}) + d_1 (u_{j+1} + u_{j-1}) + d_0 u_j]$$

where  $d_0 = 1/10$ ,  $d_1 = -3d_0/4$ ,  $d_2 = 3d_0/10$ , and  $d_3 = -d_0/20$ . The complete operator, which is fifth-order accurate, is applied as follows:

$$(14) \quad \tilde{\mathbf{A}} \frac{\partial \mathbf{Q}}{\partial x} \approx \tilde{\mathbf{A}} \delta_x^a \mathbf{Q} + |\tilde{\mathbf{A}}| \delta_x^s \mathbf{Q}$$

with

$$(15) \quad |\tilde{\mathbf{A}}| = \mathbf{X} |\mathbf{\Lambda}| \mathbf{X}^{-1}$$

where  $\mathbf{X}$  is the matrix of right eigenvectors and  $\mathbf{\Lambda}$  the matrix of eigenvalues of  $\tilde{\mathbf{A}}$ . The  $y$ -derivative operator uses the matrix  $|\tilde{\mathbf{B}}|$ , which is formed in an analogous manner. When curvilinear coordinates are used, the matrices  $|\hat{\mathbf{A}}|$  and  $|\hat{\mathbf{B}}|$  are used.

When applied to an ordinary differential equation (ODE) of the form

$$\frac{du}{dt} = f(u, t)$$

the time-marching method is given by the following:

$$(16) \quad \begin{aligned} u_{n+\alpha_1}^{(1)} &= u_n + h\alpha_1 f_n \\ u_{n+\alpha_2}^{(2)} &= u_n + h\alpha_2 f_{n+\alpha_1}^{(1)} \\ u_{n+\alpha_3}^{(3)} &= u_n + h\alpha_3 f_{n+\alpha_2}^{(2)} \\ u_{n+\alpha_4}^{(4)} &= u_n + h\alpha_4 f_{n+\alpha_3}^{(3)} \\ u_{n+\alpha_5}^{(5)} &= u_n + h\alpha_5 f_{n+\alpha_4}^{(4)} \\ u_{n+1} &= u_n + h f_{n+\alpha_5}^{(5)} \end{aligned}$$

where  $h = \Delta t$  is the time step,  $t_n = nh$ ,  $u_n = u(t_n)$ , and

$$f_{n+\alpha}^{(k)} = f(u_{n+\alpha}^{(k)}, t_n + \alpha h)$$

With  $\alpha_1 = 1/6$ ,  $\alpha_2 = 1/5$ ,  $\alpha_3 = 1/4$ ,  $\alpha_4 = 1/3$ , and  $\alpha_5 = 1/2$ , the method is sixth-order accurate for linear homogeneous ODE's and second-order otherwise. When applied to wave propagation problems together with the spatial operator given above, this method is generally somewhat more accurate than the classical fourth-order Runge-Kutta method for a given computational effort, despite its lower formal order. Furthermore, this method requires only two memory locations per dependent variable while the fourth-order Runge-Kutta method requires three. Thus this six-stage method combines excellent accuracy with low memory requirements. Its stability contour (shown in Ref. [14]) is adequate for the nonstiff problems of interest here.

### 4 Interface and boundary treatment

Our approach is to treat dielectric media with different constitutive properties as distinct subdomains coupled through appropriate interface conditions. Therefore, we

consider three distinct boundary types, an interface between different dielectrics, a boundary at the surface of a perfect conductor, and an artificial outer boundary resulting from the need for a finite domain. In each case, a locally one-dimensional characteristic formulation is used [4]. The system of equations is decomposed into characteristic variables representing incoming and outgoing waves along a direction normal to the interface or boundary. For example, for a constant- $x$  boundary at the right side of a subdomain, the incoming waves are associated with  $\tilde{\mathbf{A}}^-$  and the outgoing waves are associated with  $\tilde{\mathbf{A}}^+$ , where the matrices  $\tilde{\mathbf{A}}^\pm$  are given by

$$(17) \quad \tilde{\mathbf{A}}^\pm = \frac{\tilde{\mathbf{A}} \pm |\tilde{\mathbf{A}}|}{2}$$

Similar expressions are obtained at constant- $y$  boundaries and in curvilinear coordinates. In the latter case, the matrices  $\hat{\mathbf{A}}^\pm$  and  $\hat{\mathbf{B}}^\pm$  are formed. Upwind difference operators are then applied. The terms representing outgoing waves are differenced using conventional sixth-order one-sided and biased operators. For the incoming waves, the following fifth-order operators are used:

$$(18) \quad (\delta_x u)_1 = \frac{1}{60\Delta x} [-3u_0 - 119u_1 + 255u_2 - 240u_3 + 155u_4 - 57u_5 + 9u_6]$$

$$(19) \quad (\delta_x u)_2 = \frac{1}{60\Delta x} [9u_0 - 66u_1 + 70u_2 - 60u_3 + 75u_4 - 34u_5 + 6u_6]$$

Note that these numerical boundary schemes are different from those given in Refs. [13] and [14], which proved to be unstable on some curvilinear grids.

#### 4.1 Dielectric interfaces

At the interface between two isotropic dielectric media, the following conditions must be satisfied:

$$(20) \quad E_{t1} = E_{t2}$$

$$(21) \quad H_{t1} = H_{t2}$$

$$(22) \quad D_{n1} = D_{n2}$$

$$(23) \quad B_{n1} = B_{n2}$$

where the subscripts 1 and 2 distinguish the two media (note that the field intensities and flux densities can be double-valued on the boundary), and the subscripts  $t$  and  $n$  designate the components tangential and normal to the interface, respectively. In the TM case,  $\mathbf{E}$  and  $\mathbf{D}$  point

out of the plane and thus the third condition is satisfied automatically and the first condition simplifies to

$$(24) \quad E_{z1} = E_{z2}$$

The procedure used to enforce these interface conditions will be described for an interface lying on a line of constant  $\xi$  with the positive  $\xi$  direction pointing from medium 1 to medium 2. Generalization to other cases and to Cartesian grids is straightforward. The curvilinear grids are constructed such that the interfaces always lie along grid lines. Furthermore, the grid lines are orthogonal at boundaries and interfaces. The characteristic variables associated with outgoing waves are extrapolated from the interior of each subdomain on either side of the interface. These are coupled with the interface conditions to determine the field values on either side of the interface which are used as boundary conditions in the respective subdomains. This procedure permits the grid in each subdomain to be generated independently. This is an important consideration since the grid resolution requirements are dependent on the material properties.

In order to apply the interface conditions, we require  $D_{z1}$ ,  $D_{z2}$ ,  $B_{t1}$ ,  $B_{t2}$ ,  $B_{n1}$  and  $B_{n2}$ , where

$$(25) \quad B_t = \frac{\frac{\partial \xi}{\partial y} B_x - \frac{\partial \xi}{\partial x} B_y}{\sqrt{\frac{\partial \xi^2}{\partial y^2} + \frac{\partial \xi^2}{\partial x^2}}}$$

and

$$(26) \quad B_n = \frac{\frac{\partial \xi}{\partial x} B_x + \frac{\partial \xi}{\partial y} B_y}{\sqrt{\frac{\partial \xi^2}{\partial y^2} + \frac{\partial \xi^2}{\partial x^2}}}$$

The normal component of the magnetic flux density at the interface, which is single-valued according to equation 23, is determined using sixth-order interpolation. Thus we require four equations in order to determine  $D_{z1}$ ,  $D_{z2}$ ,  $B_{t1}$ , and  $B_{t2}$ . Two equations are provided by sixth-order extrapolation of the characteristic variables associated with waves leaving each medium. Hence we extrapolate the following quantity from medium 1 to the interface:

$$(27) \quad w_1^+ = \eta_{I1} D_{z1} + B_{t1}$$

where  $\eta_I = \sqrt{\mu/\epsilon}$ . The following quantity is extrapolated from medium 2:

$$(28) \quad w_2^- = \eta_{I2} D_{z2} - B_{t2}$$

Note that the quantities extrapolated depend on the orientation of the local  $(\xi, \eta)$  coordinate system at the interface.

The remaining two equations are provided by the interface conditions, which for this case are written as follows:

$$(29) \quad \epsilon_2 D_{z1} - \epsilon_1 D_{z2} = 0$$

$$(30) \quad \mu_2 B_{t1} - \mu_1 B_{t2} = 0$$

These four equations can be solved for  $D_{z1}$ ,  $D_{z2}$ ,  $B_{t1}$ , and  $B_{t2}$ . The Cartesian components of the magnetic flux density can then be calculated from the normal and tangential components.

## 4.2 Perfect conductors

At the surface of a perfect conductor, the component of the electric field tangential to the boundary and the component of the magnetic flux density normal to the boundary must be zero. For the TM case, this gives

$$(31) \quad D_z = B_n = 0$$

We also require  $B_t$  at the boundary. This is determined by sixth-order extrapolation of the appropriate characteristic variable from the dielectric medium to the boundary. For example, if the perfectly-conducting surface lies along a grid line of constant  $\xi$ , with  $\xi$  increasing as the boundary is approached, then  $w^+$  is extrapolated and, since  $D_z = 0$ ,

$$(32) \quad B_t = w^+$$

on the boundary, where  $B_t$  and  $w^+$  are defined in equations 25 and 27, respectively. The Cartesian components of the magnetic flux density are then determined using the fact that  $B_n = 0$ .

## 4.3 Artificial boundaries

The outer boundaries are handled using locally one-dimensional characteristic boundary conditions. As it is well known that this approach leads to significant spurious reflection, other methods are being examined. However, for the results shown below, the spurious reflections do not affect the solutions. The incident field is specified outside the computational domain. Therefore, the terms representing incoming waves are known outside the domain and the numerical boundary schemes given in equations 18 and 19 are not required at such boundaries.

# 5 Results and discussion

## 5.1 Dielectric square

We first consider the problem of electromagnetic scattering from a dielectric square. As shown in Figure 1, the domain

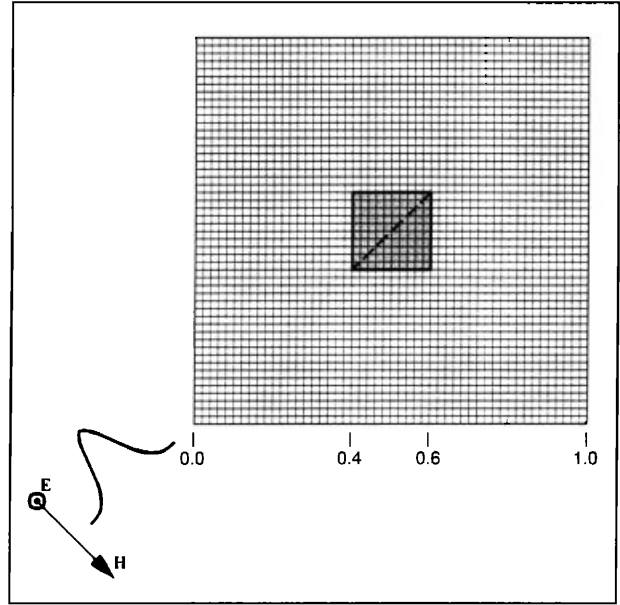


Figure 1: Sketch of dielectric square.

extends over  $0 \leq x \leq 1$ ,  $0 \leq y \leq 1$  with the square located at  $0.4 \leq x \leq 0.6$ ,  $0.4 \leq y \leq 0.6$ . The permittivity of the square is four times that of free space. With this geometry, the interface conditions are applied along grid lines even with a Cartesian grid. The corner singularities are treated by an averaging operator. Results are presented for a Gaussian pulse approaching the dielectric square at 45 degrees. The incident electric field is given by

$$E_z(x, y, t) = \exp \left[ \frac{-1}{2\sigma^2} \left( x \cos \frac{\pi}{4} + y \sin \frac{\pi}{4} + 1/2 - t \right)^2 \right]$$

with  $\sigma = 0.05$ . In all cases, the time step is chosen to produce a Courant number of unity outside the dielectric square, where the Courant number is defined as  $c\Delta t/\Delta x$  and the propagation speed,  $c$ , is unity in free space. Since the propagation speed in the square is half that in free space, the Courant number in the square is one half.

Figure 2 shows contours of the electric field intensity at  $t = 1.4$  computed using the high-accuracy finite-difference scheme on an equispaced grid with 400 intervals in each direction. Negative values of electric field intensity are shown by dashed contours. The contours obtained on a 100 by 100 grid displayed in Figure 3 show little difference from those obtained on the finer grid. In contrast, Figure 4 shows results computed using a finite-difference scheme consisting of second-order centered differences with a small amount of artificial dissipation coupled with fourth-order Runge-Kutta time marching, again on the 100 by 100 grid. These

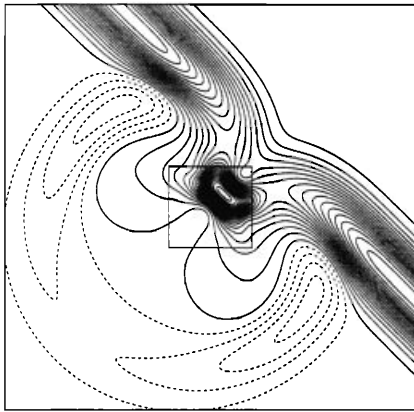


Figure 2: Contours of electric field intensity computed using high-accuracy scheme on 400 by 400 grid.

contours deviate noticeably from those shown in Figure 2, especially within the dielectric square.

The  $L_2$  norm of the error in the electric field intensity is plotted versus the grid density in Figure 5 for the high-accuracy scheme and the second-order scheme described above. The solution shown in Figure 2 is used as a reference solution in order to calculate the errors. Although this solution is not exact, its error is sufficiently low compared to those shown to provide accurate error estimates. The error produced by the high-accuracy scheme on the 100 by 100 grid (indicated by a 1 on Figure 5) is less than one-fifth of that produced by the second-order scheme on a 200 by 200 grid (indicated by a 2). For these two solutions, the high-accuracy scheme required less than one-fourth the computing time and roughly one-sixth as much computer memory as the second-order scheme. Although the high-accuracy scheme requires more computing time per grid node per time step, this is more than offset by the smaller number of nodes and the associated larger time step. The lower memory requirements result from the smaller number of nodes and the use of a low-storage time-marching method. Figure 6 compares the solutions obtained along the diagonal of the dielectric square as indicated by the dashed line in Figure 1. The superiority of the high-accuracy solution is evident. The high-accuracy solution computed on the 100 by 100 grid is even slightly more accurate than the second-order solution on the 400 by 400 grid, which required over thirty times more computing time and twenty-four times more memory.

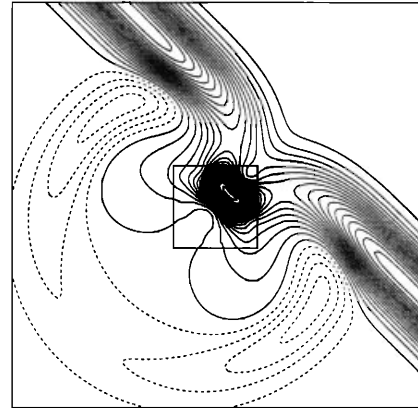


Figure 3: Contours of electric field intensity computed using high-accuracy scheme on 100 by 100 grid.

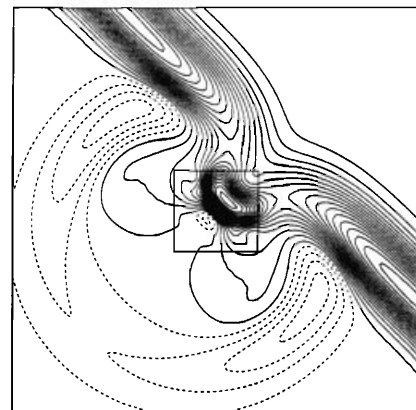


Figure 4: Contours of electric field intensity computed using second-order scheme on 100 by 100 grid.

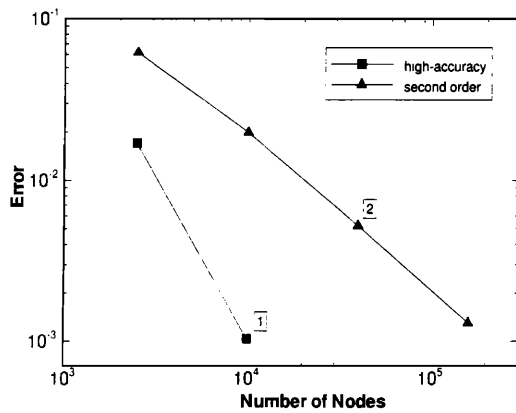


Figure 5: Error in the electric field intensity as a function of the number of nodes in the grid.

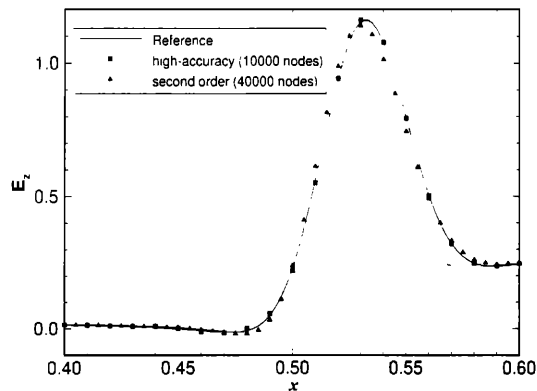


Figure 6: Electric field intensity on the diagonal of the dielectric square.

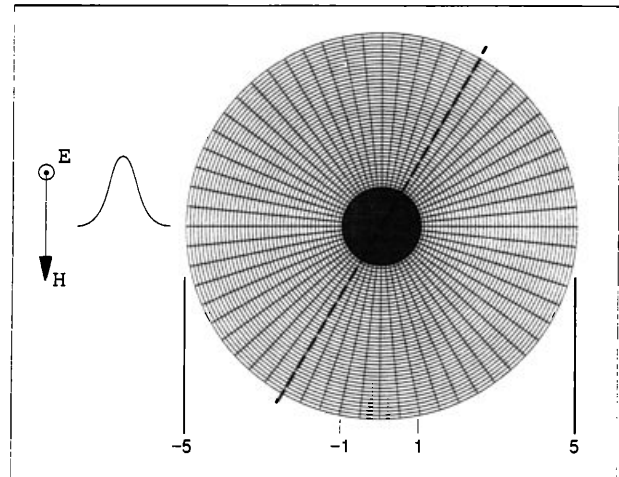


Figure 7: Sketch of perfectly-conducting cylinder.

## 5.2 Perfectly-conducting cylinder

The previous example shows the potential of the Cartesian grid approach for implementing high-accuracy schemes. Unfortunately, it is extremely difficult to develop stable and accurate boundary and interface formulations when the boundary does not lie along a grid line. One option is to impose the change in permittivity gradually [12]. However, this approach leads to significant errors which, although acceptable for a second-order formulation, preclude its use with high-accuracy operators. Other promising methods for handling interfaces include the finite-surface method [11] and the use of collar grids which overlap a Cartesian grid [5]. However, both of these approaches are difficult to extend to higher order.

We now consider an example using a curvilinear grid which consists of a pulsed waveform incident on a perfectly-conducting cylinder. The geometry and a grid are shown in Figure 7. The polar grid extends out four cylinder radii from the surface. The incident field is

$$E_z(x, y, t) = \exp \left[ \frac{-1}{2\sigma^2} (x + 15/2 - t)^2 \right]$$

with  $\sigma = 0.3$ . For all of the computations, the time step is chosen to produce a maximum Courant number of unity. Grid metrics are calculated using the same operator as is applied to the spatial derivatives.

The finest grid used has 480 grid intervals in the circumferential direction and 320 in the radial direction. The solution computed using the high-accuracy finite-difference scheme on this grid is used as the reference in determining the errors produced on coarser grids. Contours of electric field intensity in the region near the cylinder at  $t = 8.5$  are

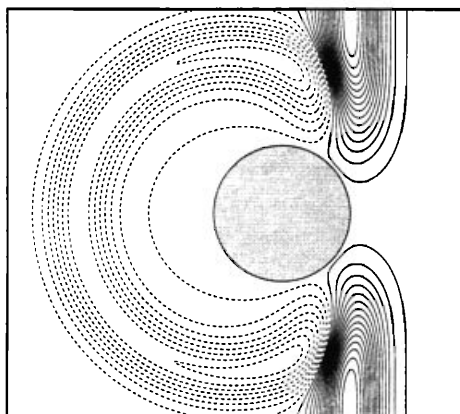


Figure 8: Contours of electric field intensity computed using high-accuracy scheme on 480 by 320 grid.

shown in Figure 8. The solution computed using the high-accuracy scheme on a 120 by 80 grid is shown in Figure 9. Agreement with the fine grid results is excellent. Note that the jagged contours in Figure 9 are caused by the contour plotting; the solution itself is smooth. Figure 10 shows that the second-order scheme produces considerable error on the 120 by 80 grid.

The electric field intensity along the dashed line in Figure 7 is plotted in Figure 11. As in the Cartesian grid example, the solution computed using the high-accuracy scheme is substantially more accurate than that computed using the second-order scheme on a grid with four times as many nodes. Figure 12 shows the  $L_2$  norm of the error in the electric field intensity along this line for several grids. We have selected this line because the error for the whole domain is dominated by that occurring in the large cells at the top and bottom of the domain. The trends shown are independent of the line chosen. The solutions shown in Figure 11 are indicated by a 1 and a 2 in Figure 12. The relative efficiency of the two schemes is virtually identical to that obtained on the Cartesian grid. The error produced by the high-accuracy scheme on the 120 by 80 grid is less than one-fourth that produced by the second-order scheme on a 240 by 160 grid. For these solutions, the computing time of the high-accuracy scheme is less than one-fourth that of the second-order scheme and the memory requirements are six times smaller. Once again, the high-accuracy solution computed on the 120 by 80 grid is slightly more accurate than the second-order solution on a grid with sixteen times as many nodes, which required over thirty-two

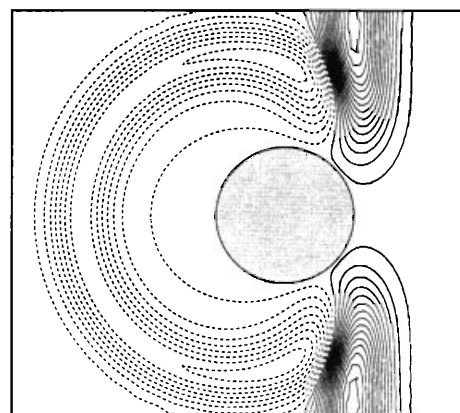


Figure 9: Contours of electric field intensity computed using high-accuracy scheme on 120 by 80 grid.

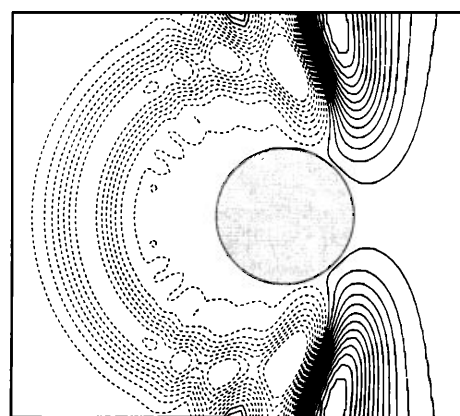


Figure 10: Contours of electric field intensity computed using second-order scheme on 120 by 80 grid.

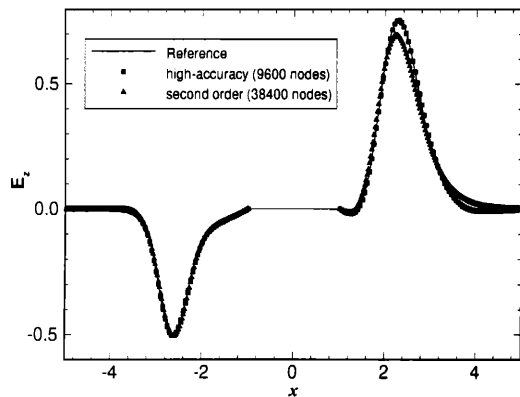


Figure 11: Electric field intensity along the dashed line in Figure 7.

times more computing time and twenty-four times more computer memory.

## 6 Conclusions

We have implemented a high-accuracy finite-difference scheme to solve numerically the two-dimensional time-domain Maxwell equations. The interface formulation preserves the high accuracy of the interior scheme. The examples presented include both scattering from an interface between media with different permittivities and from a perfectly-conducting surface. Excellent results are obtained for Cartesian and curvilinear grids. The high-accuracy scheme proved to be substantially more efficient than a second-order scheme in terms of both computing time and computer memory.

## References

- [1] D.A. Anderson, J.C. Tannehill, and R.H. Pletcher, *Computational Fluid Mechanics and Heat Transfer*, Hemisphere, New York, 1984.
- [2] G. Cohen and P. Joly, *Fourth order schemes for the heterogeneous acoustics equation*, *Comp. Meth. in Applied Mech. and Eng.*, 80, (1990), pp. 397-407.
- [3] S. Davis, *Low-dispersion finite difference methods for acoustic waves in a pipe*, *J. Acoust. Soc. Am.*, 90, (1991), pp. 2775-2781.

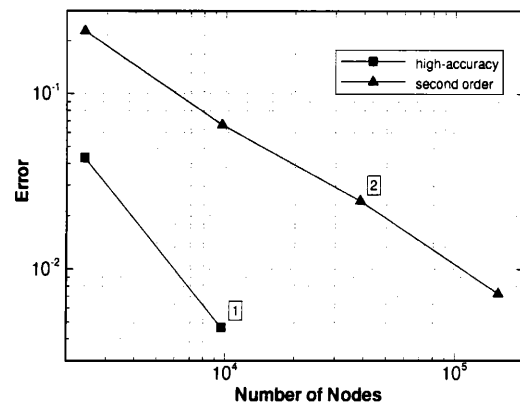


Figure 12: Error in the electric field intensity as a function of the number of nodes in the grid.

- [4] C. Hirsch, *Numerical Computation of Internal and External Flows, Vol. 2: Computational Methods for Inviscid and Viscous Flows*, Wiley, England, 1990.
- [5] T.G. Jurgens, A. Taflove, K.R. Umashankar, and T.G. Moore, *Finite-difference time-domain modeling of curved surfaces*, *IEEE Trans. Antennas Propagat.*, 40, (1992), pp. 357-366.
- [6] S.K. Lele, *Compact finite difference schemes with spectral-like resolution*, *J. Comput. Phys.*, 103, (1992), pp. 16-42.
- [7] J. Lighthill, *Report on the final panel discussion on computational aeroacoustics*, ICASE Rept. No. 92-53, (1992).
- [8] D.P. Lockard, K.S. Brentner, and H.L. Atkins, *High accuracy algorithms for computational aeroacoustics*, AIAA Paper 94-0460, (1994).
- [9] A. Taflove, *Re-inventing electromagnetics: super-computing solution of Maxwell's equations via direct time integration on space grids*, AIAA Paper 92-0333 (1992).
- [10] C.K.W. Tam and J.C. Webb, *Dispersion-relation-preserving finite difference schemes for computational acoustics*, *J. Comput. Phys.*, 107, (1993), pp. 262-281.
- [11] M. Vinokur and M. Yarrow, *Finite-surface method for the Maxwell equations in generalized coordinates*, AIAA Paper 93-0463, (1993).

- [12] M. Yarrow, J.A. Vastano, and H. Lomax, *Pulsed plane wave analytic solutions for generic shapes and the validation of Maxwell's equations solvers*, AIAA Paper 92-0016, (1992).
- [13] D.W. Zingg, H. Lomax, and H.M. Jurgens, *An optimized finite-difference scheme for wave propagation problems*, AIAA Paper 93-0459, (1993).
- [14] D.W. Zingg, H. Lomax, and H.M. Jurgens, *High-accuracy finite-difference schemes for linear wave propagation*, SIAM J. on Scientific Computing, to appear March 1996.
- [15] D.W. Zingg, E.M. Epstein, and H.M. Jurgens, *A comparison of finite-difference schemes for computational aeroacoustics*, AIAA Paper 95-0162, (1995).